PANE

P. J. Phys. 02 (01), 062 (April 2026) PANE Journal of Physics

SYNTHESIS AND DIELECTRIC PROPERTIES ANALYSIS OF POLYTHIOPHENE NANOPARTICLES

Paragjyoti Chutia*[1]

[1]*Department of Physics, DHSK College, Dibrugarh-786001, Assam, India*

*Corresponding Author: paragjyotic@gmail.com

(Received 13 September 2025; revised 3 January 2026; accepted 14 January 2026; published 6 April 2026)

Abstract: Polythiophene nanoparticles were synthesized using a cationic surfactant-assisted chemical oxidative polymerization technique. Morphological, dielectric relaxation, and AC conductivity analyses were carried out with systematically varying CTAB concentrations. HRTEM images show well-ordered nanoparticles. X-ray diffraction patterns reveal a new diffraction peak at $2\theta = 26.6^\circ$ at higher CTAB concentrations, indicating an enhancement of the conjugation length. Dielectric permittivity studies show that at lower frequencies ($< 10^5$ Hz), the relaxation is dominated by the electrode polarization effect. AC conductivity analysis suggests the presence of a correlated barrier hopping mechanism. In the scaling approach, the AC conductivity data obtained at different temperatures superimpose on one another, suggesting a temperature-invariant conduction process.

Keywords: polythiophene. Nanoparticles. dielectric permittivity. AC conductivity. electric modulus.

PACS: 61.10.Nz, 68.37.Lp, 77.22.Ch

1 Introduction

Polymers with heteroaromatic rings have received an enormous deal of interest among researchers in the last two decades [1, 2]. Electronic properties of conjugated conducting polymers can be manipulated through changing doping level and modifying its structure from insulating to metal [3]. Conducting polymers are widely used in different technological applications such as electrodes, sensors, actuators, light emitting diodes, etc. [4, 5]. Among the diversity of intrinsically conducting polymers polythiophene (PTh) is widely studied because its promising electronic and optical properties, natural constancy against oxygen and moisture, structural versatility, high conductivity and wide commercial applications [6]. Polythiophene can be obtained from the polymerization of thiophene through chemically, photo-chemically, electrochemically [7, 8]. Some notable applications of typical PTh derivatives are molecule-based devices, rechargeable battery electrodes, light-emitting diodes, chemical and optical sensors etc. [9, 10]. Among the family of conjugated conducting polymers, Polythiophene and its derivatives have received significant interest among scientist owing to their superior stability, ease of structural change, flexible optical and electrochemical behaviors [11]. The dielectric and modulus formalism can be employed to understand the charge transport process in disordered systems. The movement of charge carriers and orientations of dipoles in polymer determines AC conductivity and dielectric relaxation. Interfacial polymerization in disordered polymeric materials or in polymeric composite materials arises because of dopant ions, fillers, or other impurities present in the system. At low frequencies the interfacial polarization is covered by the conductivity and high permittivity values [12]. The charge carriers relaxation process and different polarization mechanism present in a system can be understood through modulus formalism and dielectric formalism, respectively. The presence of charge carrier hopping mechanism in conducting polymers, results the conductivity relaxation which is different from the dielectric relaxation in common polymers. The electrode polarization outcomes the high values of permittivity at lower frequencies which get concealed in the modulus formalism [13].

Dielectric and AC conductivity of Polyaniline, Polypyrrole and PEDOT nanostructures have been widely studied by many research groups in recent years [14–16] but synthesis and dielectric properties study of polythiophene

nanostructured systems are limited. The present paper investigates the dielectric and charge transport properties of PTh nanoparticles. Further, the effect of CTAB concentrations on structural, dielectric and transport properties has also been studied.

2 Experimental

2.1 Materials

Sigma Aldrich company prepared thiophene monomer has been used for synthesis of polythiophene. The oxidant ferric chloride ($FeCl_3$), chloroform, surfactant N, N, N-Trimethyl-1-hexadecanaminium bromide (CTAB), methanol and acetone were purchased from Merck.

2.2 Preparation of polythiophene nanoparticles

Cationic surfactant-assisted chemical oxidative polymerization procedure has been employed to synthesis Polythiophene (PTh) nanoparticles. In present synthesis procedure thiophene monomer (0.024 mol) and surfactant CTAB (0.003 mol) were dissolved in $CHCl_3$ (20 ml) and kept under stirring for 15 m. $FeCl_3$ (0.0055 mol) was added in $CHCl_3$ (70 ml) and poured drop wise to the monomer-surfactant solution under stirred conditions [17]. The synthesis process was being carried out at room temperature and kept stirring for 24 h. The obtained dark-brown precipitates were first subjected to centrifugation to separate the solid product from the reaction medium. The supernatant containing unreacted species was carefully removed, and the collected final product was repeatedly washed with deionized water and ethanol to ensure effective removal of residual reactants and by-products. Each washing step was followed by centrifugation. Finally, the purified nanoparticles were dried under vacuum at 70°C for 6 h to remove physically adsorbed moisture and residual solvents, yielding the final purified product. For CTAB concentrations 1 mmol, 2 mmol, 3 mmol, 4 mmol and 5 mmol the samples are named as C1, C2, C3, C4 and C5, respectively. Block diagrams of the synthesis and purification steps are depicted in Fig. 1(a) and Fig. 1(b), respectively.

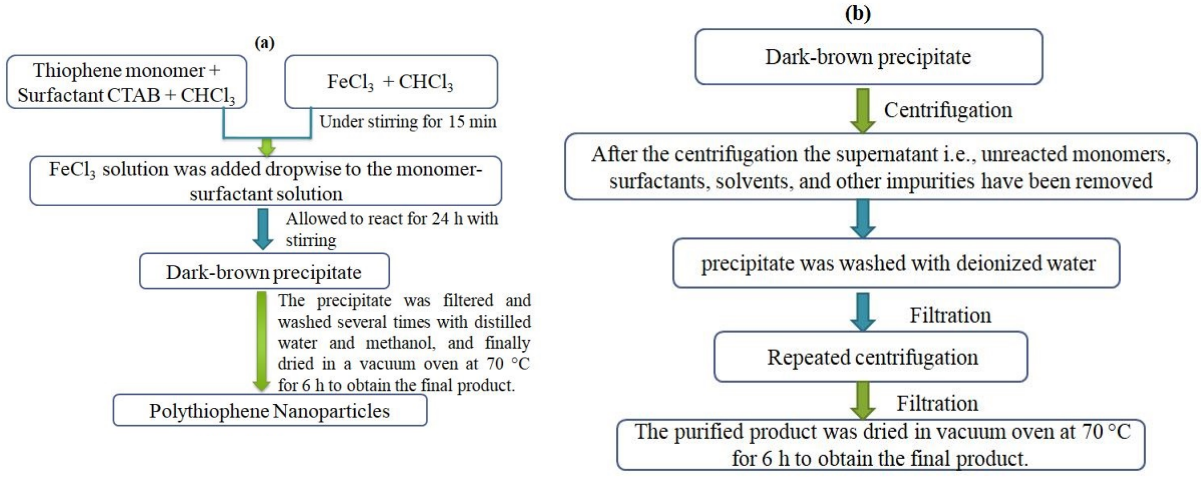

Figure 1: Block diagram of (a) synthesis of polythiophene nanoparticles and (b) purification steps of obtained dark-brown polythiophene nanoparticles precipitates.

2.3 Characterization

The shape and size of the PTh nanoparticles were observed with high-resolution transmission electron microscope (HRTEM, JEM-2100, 200 kV, Jeol). Bruker D8 Advance X-ray diffractometer was employed for X-ray diffraction analysis. Nicolet Impact I-410 FTIR spectrometer was being used to study FTIR spectra between 400 cm^{-1} to 4000 cm^{-1}. The thermal measurement was carried out by employing the Perkin Elmer thermal analyzer TGA 6000 in nitrogen environment from room temperature to $\sim$ 900°C at heating rate of 10°C min^{-1}. HIOKI-LCR

meter (frequency range: 42 Hz - 5 MHz) was being used for Dielectric measurements within temperature of 303 K - 363 K.

3 Results and Discussion

3.1 HRTEM study

HRTEM images of PTh samples C1 and C5 are depicted in Fig. 2(a & b) The HRTEM micrographs show the formation of fairly well-ordered spherical PTh nanoparticles. The diameter of the nanoparticles varies from 10 to 20 nm for sample C1 (Fig. 2(a)) and 2 to 6 nm for sample C5 (2(b)). From the HRTEM micrographs, it is seen that there is a reduction of particle size with increasing CTAB concentration. At high concentrations, the surfactant CTAB molecules surround the PTh nanoparticle which prevents the access of thiophene monomers to nanoparticles inhibiting the secondary growth during polymerization resulting in a smaller diameter of PTh nanoparticles [18].

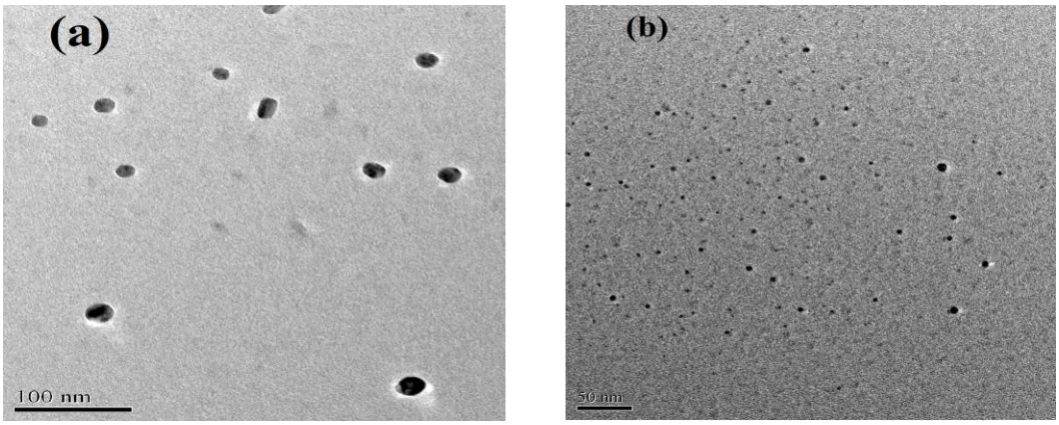

Figure 2: HRTEM micrographs of PTh nanoparticles (a) C1 and (b) C5

3.2 XRD study

Fig. 3(a) depicts XRD patterns of synthesized PTh nanoparticles. Broad diffraction peak in the 2θ range of $15^\circ - 25^\circ$ is observed for all the samples. The amorphous diffraction hump is attributed to the intermolecular $\pi - \pi$ stacking energies [19]. From the figure, it is observed that at higher CTAB concentration (C5) a new peak at around $2\theta = 26.6^\circ$ appears, which can be ascribed to the enhancement of π-conjugation length of the PTh nanoparticles [20].

3.2.1 Estimation of crystallite size (D) and lattice strain (ϵ) by using single-line approximation method

Crystallite size and strain results peak broadening and XRD patterns can be used to determine these parameters [21]. Instrumental and sample-dependent effects results the width of diffraction peak. Well annealed Cu powder was used to eliminate the instrumental broadening [22]. The single-line approximation method has been carried out employing the Voigt function considering that the Cauchy component β_C^f is due to size effect, whereas β_G^f is solely due to micro-strain [23]. According to the method, the crystallite size or domain size and the maximum value of the strain can be expressed as [24],

$$D = \frac{\lambda}{\beta_C^f \cos\theta} \tag{1}$$

and

$$\epsilon = \frac{\beta_G^f}{4\tan\theta} \tag{2}$$

In this report, although the peaks appear broad due to the amorphous nature of polythiophene, a discernible hump within the 2θ values of 15° to 30° becomes more defined upon doping, suggesting the onset of short-range

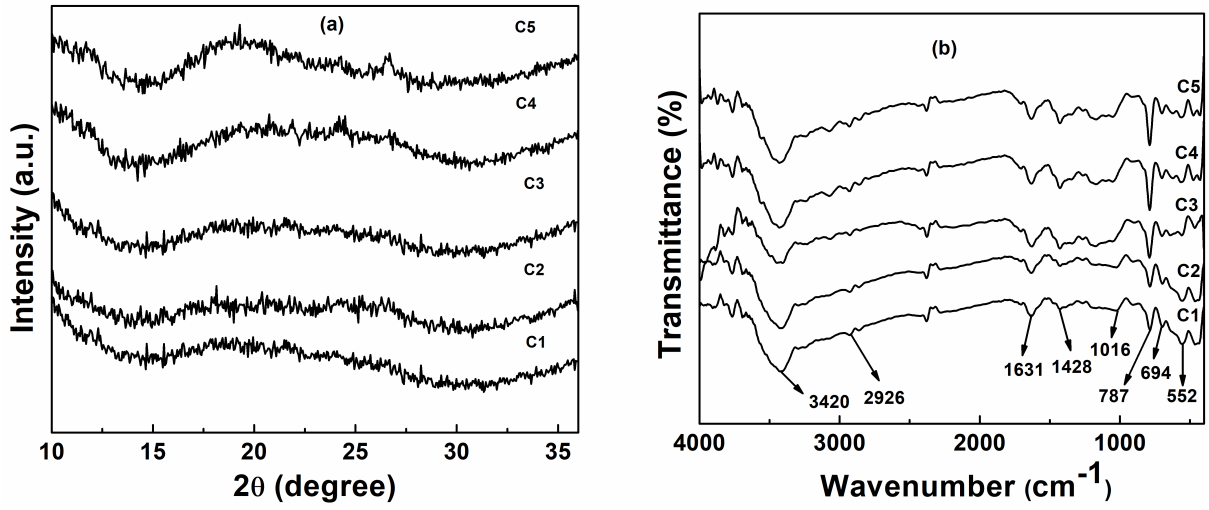

Figure 3: (a) XRD patterns of PTh nanoparticles with varying CTAB concentration and (b) FTIR spectra of PTh nanoparticles for different CTAB concentrations.

ordering of polymer chains Crystallite size and strain can be obtained from the single-line approximation method. Crystallite size (D) and strain (ϵ) values obtained from X-ray diffraction analysis is presented in Table 1. With increasing CTAB concentration, crystallite size decreases and it can be ascribed to a decrease in nanoparticles size as confirmed by the HRTEM micrograph. Dislocations and point defects may results in strain in the PTh nanoparticles [25], which are found to increase with increasing CTAB concentration. The increase of strain with increasing CTAB concentration results due to a decrease of particle size as confirmed by HRTEM.

Sample name	D(Å)	ϵ	I_{sym}/I_{asym}
C1	8.32	0.00813	0.96
C2	8.12	0.00934	0.89
C3	6.75	0.01101	0.68
C4	4.61	0.01223	0.65
C5	2.12	0.01342	0.62

Table 1: Structural parameters for the samples C1, C2, C3, C4 and C5

3.3 FTIR analysis

Fig. 3(b) represents the FTIR spectra of PTh nanoparticles for different CTAB concentrations. The O-H stretching absorption band arises at 3420 cm^{-1} and 2926 $^{-1}$ result from of water in KBr [26] and aliphatic C-H stretching vibration [27]. The C=C asymmetric and symmetric stretching vibration modes of the thiophene ring are observed at 1631 and 1428 cm^{-1}, respectively. The bands at 1016, 787, 694 and 552 cm^{-1} are attributed to the C-H in-plane deformation, C-H out-of-plane deformation, C-S bending and C-S-C ring deformation, respectively [17, 27]. The area intensity ratio, Isym/Iasym of the bands at 1428 $^{-1}$ and 1631 cm^{-1} give information about the chain length of the polymer. The lower value of the intensity ratio indicates the longer chain length [28]. From the calculated intensity ratio (I_{sym}/I_{asym}) of PTh nanoparticles, it has been observed that the intensity ratio (I_{sym}/I_{asym}) shows a decreasing trend at higher CTAB concentration, suggesting an increase in conjugation length. The obtained values are listed in Table 1. The sharp asymmetric band at 1631 cm^{-1} signifies that PTh nanoparticles are composed of long coplanar conjugated segments [28]. The increasing sharpness of the asymmetric band with increasing CTAB concentration indicates the increase of coplanar conjugated segments.

3.4 Thermal analysis

The degradation behavior of the PTh nanopartices were studied using thermogravimetric analysis (TGA). The thermogravimetric plots of PTh nanoparticles is presented in Fig. 4. The TGA studies indicate three steps of degradation. Evaporation of physically adsorbed water molecules in the polymer chains results the first step weight losses in the temperature range $30 - 150°$C. The weight loss observed in the temperature range of $330 - 495°$C is ascribed to the elimination of surfactant from the polymer shackle. The third step of weight loss begins at $495°$C due to the degradation of polymer backbone [29]. From the thermogram spectra, an enhancement of thermal stability with increasing CTAB concentration is observed. For sample C1 the weight loss is 17% up to the temperature of $495°$C whereas for sample C5 it is decreased to 11%. As confirmed by XRD analysis, the enhancement of thermal stability for higher CTAB concentration may be due to the increased crystallinity and crystallite size of the PTh nanoparticles.

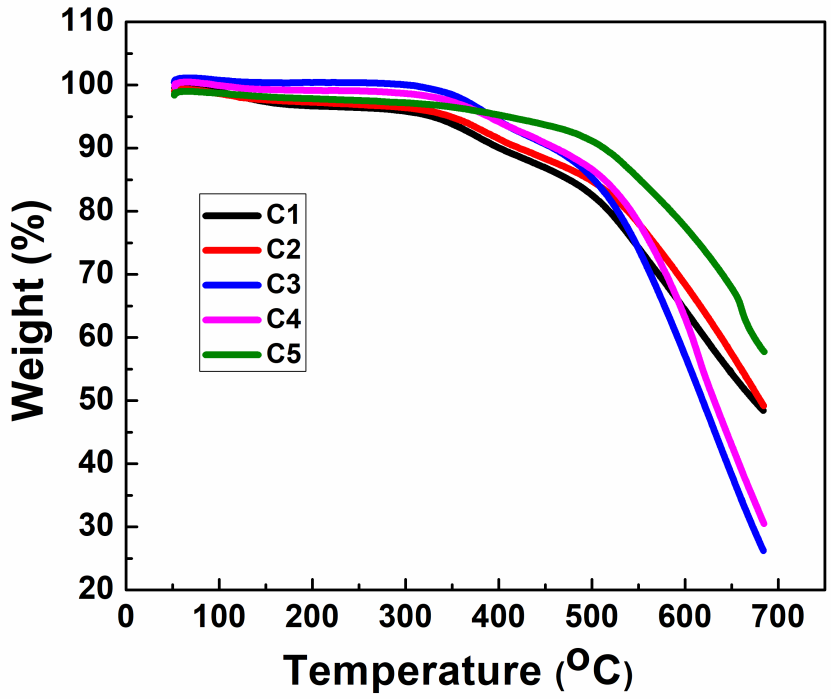

Figure 4: TGA plots of PTh nanoparticles for different CTAB concentration.

3.5 Dielectric properties analysis

The alternating electric field can polarize an electrical medium and which can be understood through the study of dielectric properties. Under the application of alternating electric field to a dielectric the polarization occurs because of displacement of electrical charges from their equilibrium. Eq. (3) describes how the dielectric parameter changes with frequency [22],

$$\epsilon^*(\omega) = \epsilon'(\omega) - i\epsilon''(\omega). \tag{3}$$

here $\epsilon'(\omega)$ and $\epsilon''(\omega)$ represents the real and imaginary components of the complex dielectric permittivity $\epsilon^*(\omega)$, respectively. Here $\epsilon'(\omega)$ measured the energy stored and the amount of energy dissipated can be obtained from $\epsilon''(\omega)$. The values of $\epsilon'(\omega)$ and $\epsilon''(\omega)$ can be obtained from the expressions,

$$\epsilon'(\omega) = \frac{Cd}{\epsilon_o A} \tag{4}$$

and the imaginary part $\epsilon''(\omega)$ as,

$$\epsilon''(\omega) = \epsilon'(\omega) \tan\delta(\omega) \tag{5}$$

where d and A represents thickness and area of the pellet, respectively. ϵ_o and $\tan\delta(\omega)$ are the permittivity in free space and loss tangent, respectively. Fig. 5(a) shows the plot of ϵ' as a function of frequency for PTh nanoparticles synthesized with varying CTAB concentrations at ambient temperature. The enhanced $\epsilon'(\omega)$ at low frequencies ($< 10^5$ Hz) due to the space-charge polarization resulting from interfacial charge buildup at the sample–electrode interfaces [30].

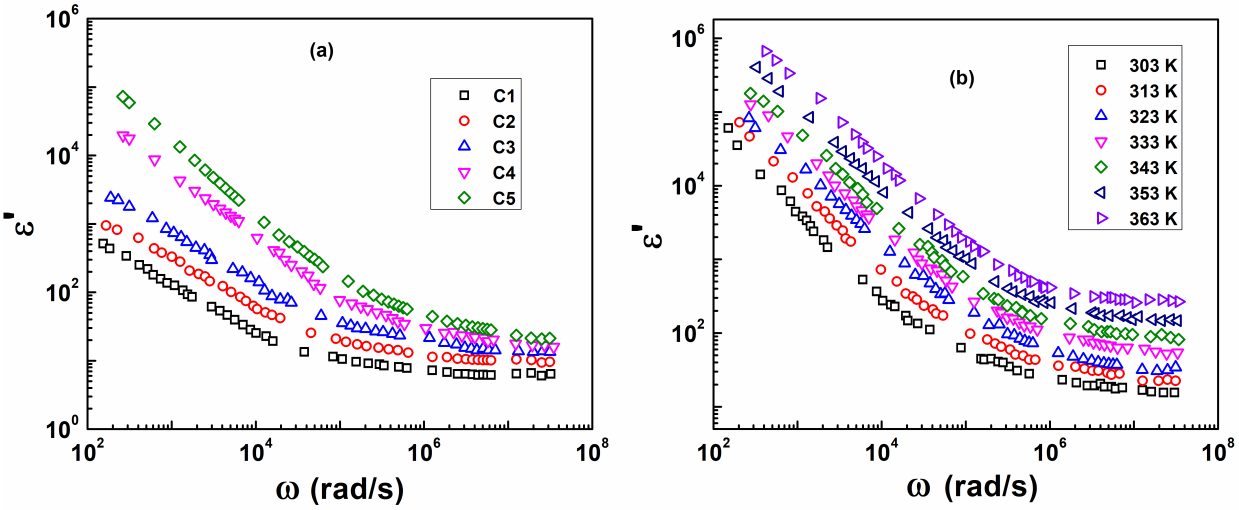

Figure 5: (a) Frequency dependence real permittivity (ϵ') of PTh nanoparticles for different CTAB concentrations at ambient temperature and (b) ϵ' vs. ω for C5 in the temperature range 303 K-363 K.

Fig. 5(b) depicts the frequency-dependent variation of $\epsilon'(\omega)$ for sample C5 at different temperatures. An increase in $\epsilon'(\omega)$ with rising temperature is observed, which is ascribed to enhanced dipolar orientation induced by greater thermal energy at elevated temperatures [31]. At higher temperatures, a pronounced increase in the dielectric constant is evident, resulting from enhanced total polarization within the system. This enhancement is attributed to the activation of both induced dipoles and thermally stimulated trapped charge carriers. With increasing temperature, the thermal energy imparted to the system facilitates polymer chain mobility, thereby reducing pinning effects that otherwise restrict charge carrier transport. The enhanced mobility promotes greater charge carrier participation in relaxation processes at a given frequency. Accordingly, the combined effects of improved dipolar orientation and increased charge carrier contribution lead to an overall rise in the dielectric constant with temperature. Conversely, at lower temperatures, restricted thermal energy suppresses both charge carrier mobility and polarization, yielding a reduced dielectric constant (ϵ') [32, 33].

3.6 Charge carriers' relaxation analysis

The dielectric permittivity only cannot explain the charge carriers' relaxation process for dielectric materials having considerable DC conductivity contribution. Charge carriers' relaxation and conduction mechanisms can be studied through the framework of Modulus formalism [34]. The complex modulus (M^*) can be articulated as,

$$M^*(\omega) = \frac{1}{\epsilon^*} = M'(\omega) + M''(\omega) \tag{6}$$

Real (M') and imaginary (M'') parts of modulus can be written as follows,

$$M'(\omega) = \frac{\epsilon'(\omega)}{\epsilon'^2(\omega) + \epsilon''^2(\omega)} \tag{7a}$$

$$M''(\omega) = \frac{\epsilon''(\omega)}{\epsilon'^2(\omega) + \epsilon''^2(\omega)} \tag{7b}$$

Fig. 6 shows the M' vs. ω plot for different CTAB concentrations at ambient temperatures. From the figure, it has been observed a very low value of M' towards lower frequency region and almost approaches zero values. For all

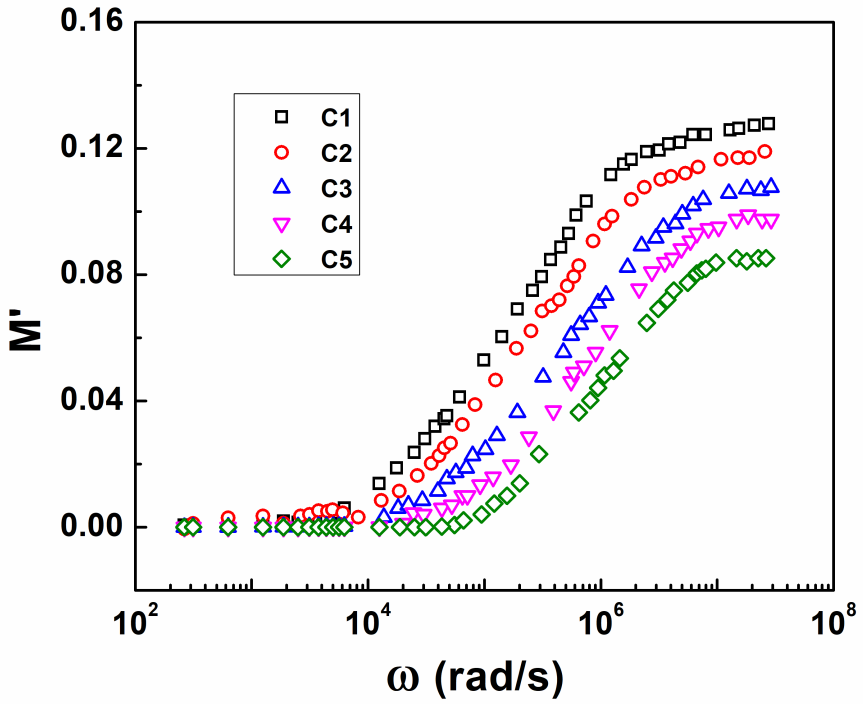

Fig. 6

Figure 6: Frequency dependence real modulus (M') for different CTAB concentrations at ambient temperature.

the different CTAB concentrations M' shows a increasing trend with frequency and reach a maximum constant value of M_∞ for frequencies $>$ 107 rad/s. The presence of such behavior indicates that the charge transport is taking place through long-range motion of charge carriers. The frequency dependent imaginary moduli M'' for different CTAB concentrations and for different temperatrures for sample C5 are depicted in Figs. 7(a) and 7(b). From figures 7(a & b) it is observed a distinct charge carriers' relaxation peak has been observed for all the CTAB concentrations and at different temperatures for sample C5 and the relaxation peak shifts towards higher frequency for both the cases. The increase of dc conductivity may be the reason of shifting the relaxation peak towards higher frequency and it can be explained according to the relation [35],

$$\sigma = \frac{\epsilon_o \omega_c}{M''} \tag{8}$$

where ω_c is the relaxation frequency. In modulus formalism, the relaxation peaks corresponding to the switching of DC to AC conductivity under an alternating electric field [36]. The transition from long-range to short-range motion of the charge carriers is represented by the relaxation frequency (ω_c) according to relation $\omega_c \tau_c = 1$, where τ_c is the conductivity relaxation time [37]. The relaxation peak shift toward high frequency side with increasing temperature or dopant concentration suggests a decrease in relaxation time. This indicates the faster response to the external electric field, resulting the enhanced mobility or rapid polarization processes. With increasing temperature, thermal energy facilitates charge-carrier hopping between localized states by reducing potential barriers, thereby improving charge transport. Similarly, increasing CTAB concentration may lead to improved particle dispersion, reduced interfacial polarization, and creation of additional conducting pathways, all of which contribute to higher conductivity and faster relaxation dynamics.

The scaling analysis was carried out for the sample C5 in the measured temperature range of 303-363 K from the plot (M''/M''_{max}) vs. $\log(\omega/\omega_c)$ as shown in Fig. 8. Formation of single master curve suggests that the conductivity relaxation mechanism is temperature independent [38].

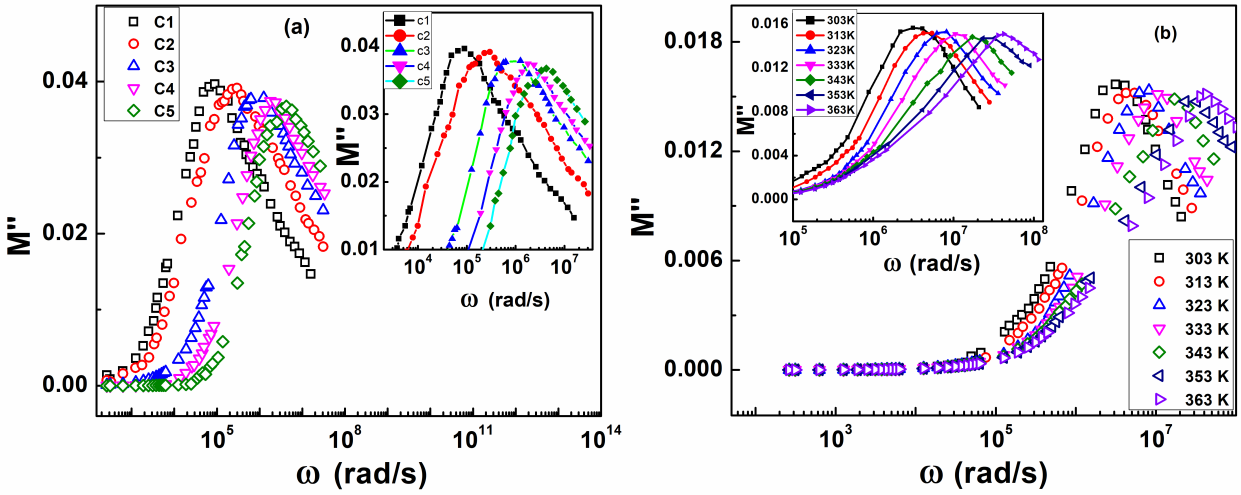

Figure 7: Frequency dependence (a) Imaginary modulus (M'') at ambient temperature for different CTAB concentration and (b) Imaginary modulus (M'') at different temperature for the sample C5.

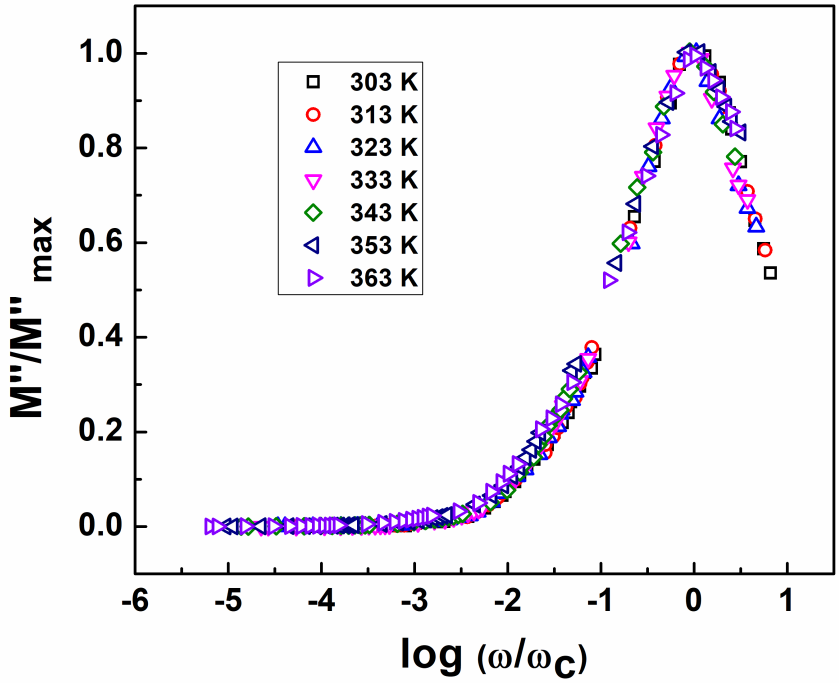

Figure 8: Scaling behavior of imaginary modulus (M'') at different temperature for the sample C5.

3.7 AC conductivity analysis

The ac conductivity can be calculated from the following expression [39],

$$\sigma(\omega) = G(\omega)\frac{d}{A} \tag{9}$$

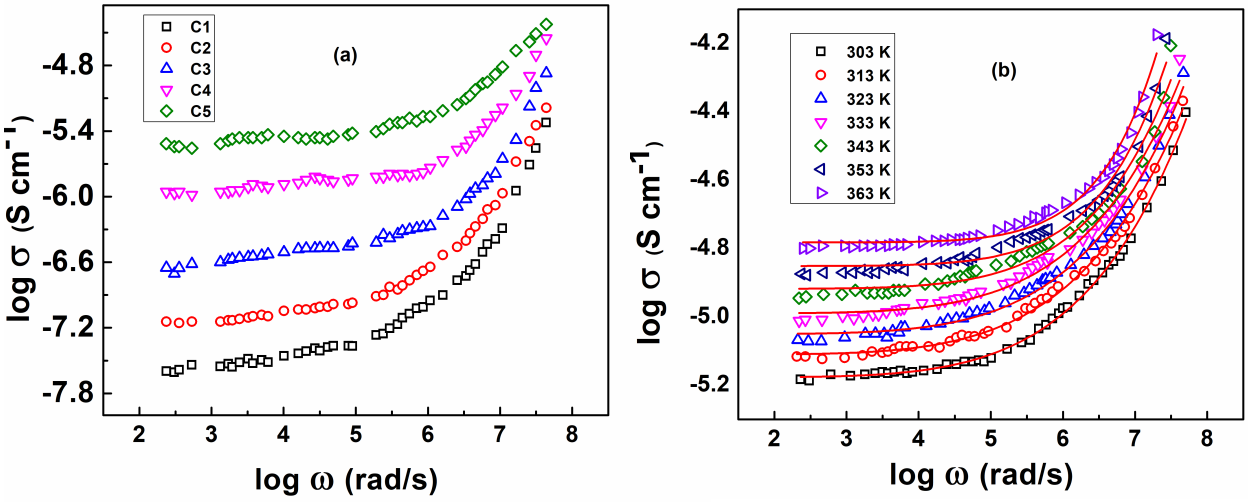

Figure 9: Plot of AC conductivity (a) for different CTAB concentration at ambient temperature and (b) for sample C5 at different temperatures (303 K - 363 K).

Here, $G(\omega)$ represents conductance. Thickness and cross-sectional area of the sample represented by d and A, respectively. Fig.9(a) depict the room temperature frequency-dependent total conductivity for different CTAB concentrations. The AC conductivity shows increasing trend frequency as well as with increasing CTAB concentrations. The total conductivity shows a increasing trend with CTAB concentrations which can be attributed to the enhanced structural ordering in the nanoparticles. Fig.9(b) shows the temperature dependent AC conductivity for sample C5. The frequency independent plateau observed in the lower frequency region arises because of DC conductivity. The shifting of plateau region towards higher frequency suggests the enhancement of DC conductivity [40].

For a particular temperature the $\sigma_{tot}(\omega)$, can be presented as follows,

$$\sigma_{tot}(\omega) = \sigma_o + \sigma(\omega) \tag{10}$$

here σ_o denotes the frequency independent conductivity. $\sigma(\omega)$ increases with frequency for amorphous semiconductor and disordered system, and follows a power law

$$\sigma(\omega) = A\omega^s \tag{11}$$

$$s = \frac{d\ln\sigma(\omega)}{d\ln\omega} \tag{12}$$

where the constant A depends on temperature. The value of frequency exponent s lies within the limit of 0 to 1. The slope $\log\sigma(\omega)$ versus $\log\omega$ plot gives the value of s [40]. For the sample C5 the values of s lie between $0.62 - 0.37$. The conduction mechanisms in disordered systems can be explained with the help of different proposed theoretical models. The behavior of frequency exponent with temperature established the type of conduction mechanism present. The decrease of s with temperature (Fig. 10(a)) implies that the charge transport is taking place through CBH mechanism. This indicates that higher temperatures facilitate carrier hopping between localized states, reducing the effective barrier height. The similar decreasing trends with temperature have been observed for the other samples as well. According to CBH model variation s with temperature is expressed as [41, 42],

$$s = 1 - \frac{6kT}{W_M - kT\ln\left(\frac{1}{\omega\tau_c}\right)} \tag{13}$$

Here W_M and τ_c represents polaron binding energy and characteristic relaxation time, respectively. In the first approximation, Eq. (13) leads to the form,

$$1 - s = \frac{6kT}{W_M} \tag{14}$$

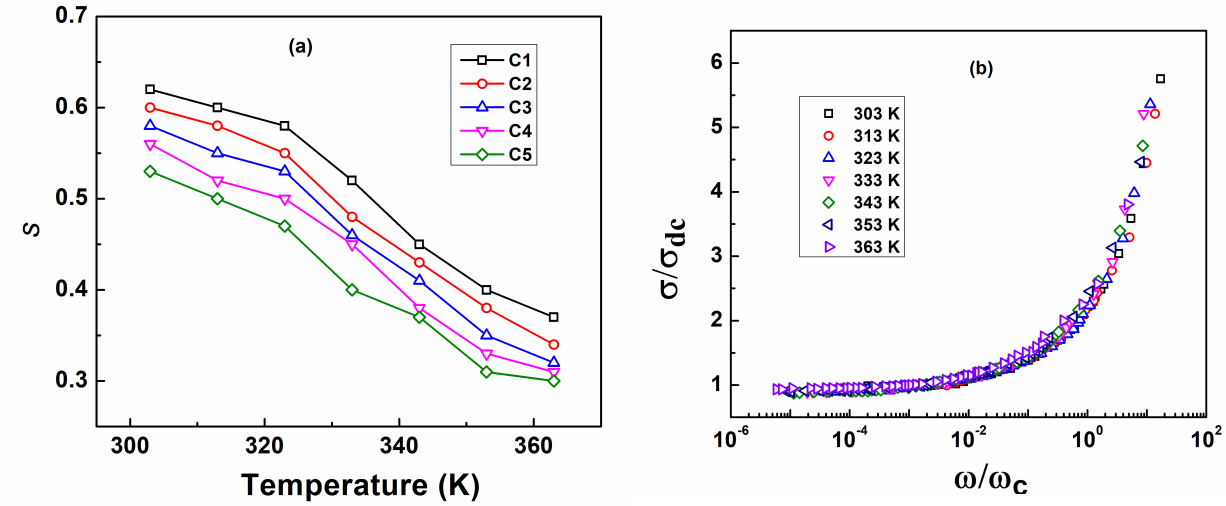

Figure 10: (a) Frequency exponent (s) vs. temperature (T) for the samples C1, C2, C3, C4 and C5 and (b) Scaling behavior of (σ/σ_{dc}) vs. (ω/ω_c) at various temperature for the sample C5.

The calculated values of polaron binding energy (W_M) are tabulated in Table 2. From the obtained values of binding energy it can be ascribed that polarons are the major charge carriers [42]. With increasing temperature, thermally activated carriers hop more easily between localized states due to the reduction of the effective barrier height. The structural modifications caused during synthesis greatly influenced on binding energy. Nanoparticles having higher structural order exhibit lower W_M values. This reduction in W_M suggest the improved of connectivity between the polymer chain networks, which results smaller separation between localized states and reduces the Coulombic interaction barriers. As a result, charge carriers require less activation energy to hop between energetically correlated sites.

Sample name	W_M(eV)
C1	0.41
C2	0.39
C3	0.37
C4	0.35
C5	0.33

Table 2: Values of W_M calculated from the ac conductivity data at 303 K for 100 Hz.

The AC conductivity is a powerful tool for understanding the dynamic processes occurring in solids, particularly in disordered materials. The time-temperature superposition principle (TTSP) plays a key role in understanding these dynamics. The single master curve obtained at different temperature leads to a scaling law known as the time temperature superposition principle [43]. The principle is based on the idea that the system behaves similarly at different temperatures but at different characteristic timescales.

The ac conductivity $\sigma(\omega)$ follows a scaling relation which can be described by the relation [37],

$$\frac{\sigma(\omega)}{\sigma_{dc}} = 1 + \left(\frac{\omega}{\omega_c}\right)^s \tag{15}$$

where, exponent s is a constant and ω_c is the characteristic frequency. This equation predicts that $\sigma(\omega)$ starts to increase as the applied frequency crosses the characteristic frequency ω_c. The values of σ_{dc}, ω_c and s have been obtained from the best fitted curves at different temperatures.

Fig. 10(b) depicts the conductivity master plot of the sample C5 for different temperatures. Here conductivity axis is scaled with respect to σ_{dc} and the frequency axis with respect to the characteristic frequency ω_c. The formation of single master curve (Fig. 10(b)) at different temperatures suggests that conduction mechanism of charge

carriers in the material is independent of temperature, and that the material is governed by universal relaxation processes [44].

4 Conclusions

In summary, we have synthesized PTh nanoparticles by the chemical oxidative polymerization method and dielectric properties are studied with varying frequency and temperature. HRTEM images confirm the formation of well-ordered nanoparticles. The new diffraction peak at $2\theta = 26.6^\circ$ in the XRD pattern at higher CTAB concentration suggest the enhancement of polymer chains ordering. In FTIR spectra the decrease of intensity ratio (I_{sym}/I_{asym}) of the band 1428 and 1631 cm^{-1} for higher CTAB concentration results due to enhancement of conjugation length. The plateau region shift towards higher frequency in the ac conductivity with increasing CTAB concentration and temperature suggest the enhancement of DC conductivity contribution. Imaginary modulus peak shifts towards higher frequency suggest the increase of conductivity. The obtained values of binding energy suggest that polarons are the major charge carriers in this system. The temperature dependent behavior of frequency exponent suggests that the charge transport is taking place through a correlated barrier hopping mechanism

References

[1] A. Javadi, A. Shockravi, M. Koohgard, A. Malek, F. A. Shourkaei, and S. Ando, European Polymer Journal **66**, 328 (2015).

[2] B. C. Roy, M. D. Gupta, L. Bhowmik, and J. K. Ray, Bulletin of Materials Science **24**, 389 (2001).

[3] K. Gupta, P. Jana, and A. Meikap, Synthetic Metals **160**, 1566 (2010).

[4] V. Q. Trung, T. T. T. Duong, N. T. Dua, N. N. Linh, L. D. Cuong, D. P. Thao, V. K. Huy, N. H. H. Phuong, N. Hien, D. K. Linh, V. Q. Manh, N. T. Chinh, T. Hoang, and L. V. Meervelt, Designed Monomers and Polymers **25**, 136 (2022).

[5] N. Asim, S. Radiman, and M. Bin Yarmo, Materials letters **62**, 1044 (2008).

[6] L. Groenendaal, F. Jonas, D. Freitag, H. Pielartzik, and J. R. Reynolds, Advanced materials **12**, 481 (2000).

[7] D. Iarossi, A. Mucci, L. Schenetti, R. Seeber, F. Goldoni, M. Affronte, and F. Nava, Macromolecules **32**, 1390 (1999).

[8] C. Wochnowski and S. Metev, Applied Surface Science **186**, 34 (2002).

[9] J. Shen, M. Kashimoto, T. Matsumoto, A. Mori, and T. Nishino, Polymer Journal **52**, 1273 (2020).

[10] S. S. Gursoy, A. Yildiz, G. C. Cogal, and O. Gursoy, Open Chemistry **18**, 974 (2020).

[11] N. N. Linh, T. T. T. Duong, N. Hien, and V. Q. Trung, Vietnam Journal of Chemistry **58**, 1 (2020).

[12] P. Hedvig, *Dielectric spectroscopy of polymers* (Akademiai Kiado, 1977).

[13] H.-T. Lee, C.-S. Liao, and S.-A. Chen, Die Makromolekulare Chemie: Macromolecular Chemistry and Physics **194**, 2443 (1993).

[14] A. Sunilkumar, S. Manjunatha, Y. Ravikiran, M. Revanasiddappa, M. Prashantkumar, and T. Machappa, Polymer Bulletin **79**, 1391 (2022).

[15] Y. A. Kulakarni, M. Jagadeesh, S. Jambaladinni, H. S. Kumar, M. Vasanthkumar, and S. Shivakumara, Journal of Materials Science: Materials in Electronics **31**, 7226 (2020).

[16] J. G. Raja, M. B. Ahamed, C. M. Hussain, and P. Era, Journal of Materials Science: Materials in Electronics **33**, 22883 (2022).

[17] S. R. P. Gnanakan, M. Rajasekhar, and A. Subramaniaa, International Journal of Electrochemical Science **4**, 1289 (2009).

[18] X. G. Li, J. Li, and M. R. Huang, Chemistry–A European Journal **15**, 6446 (2009).

[19] Y. Li, G. Vamvounis, and S. Holdcroft, Macromolecules **35**, 6900 (2002).

[20] X. G. Li, J. Li, Q. K. Meng, and M. R. Huang, The Journal of Physical Chemistry B **113**, 9718 (2009).

[21] K. Venkateswarlu, A. C. Bose, and N. Rameshbabu, Physica B: Condensed Matter **405**, 4256 (2010).

[22] S. Banerjee and A. Kumar, Journal of Applied Physics **109** (2011).

[23] T. H. de Keijser, J. I. Langford, E. J. Mittemeijer, and A. B. P. Vogels, Journal of Applied Crystallography **15**, 308 (1982).

[24] P. Saini, V. Choudhary, K. Sood, and S. Dhawan, Journal of Applied Polymer Science **113**, 3146 (2009).

[25] B. Warren and B. Averbach, Journal of Applied Physics **21**, 595 (1950).

[26] H. Gao, T. Jiang, B. Han, Y. Wang, J. Du, Z. Liu, and J. Zhang, Polymer **45**, 3017 (2004).

[27] A. Gök, M. Omastová, and A. G. Yavuz, Synthetic Metals **157**, 23 (2007).

[28] M. Akimoto, Y. Furukawa, H. Takeuchi, I. Harada, Y. Soma, and M. Soma, Synthetic Metals **15**, 353 (1986).

[29] F. Ouhib, R. C. Hiorns, R. de Bettignies, S. Bailly, J. Desbrières, and C. Dagron-Lartigau, Thin Solid Films **516**, 7199 (2008).

[30] P. Chutia and A. Kumar, Physica Status Solidi (A) **212**, 2727 (2015).

[31] T. A. Hanafy, Journal of Applied Physics **112**, 034102 (2012).

[32] E. Matveeva, R. Calleja, and V. Parkhutik, Electrochimica Acta **41**, 1351 (1996).

[33] B. G. Soares, M. E. Leyva, G. M. Barra, and D. Khastgir, European Polymer Journal **42**, 676 (2006).

[34] M. M. Ayad and E. A. Zaki, Journal of Applied Polymer Science **110**, 3410 (2008).

[35] M. G. Han and S. S. Im, Journal of Applied Polymer Science **82**, 2760 (2001).

[36] D. Almond, A. West, and R. Grant, Solid State Communications **44**, 1277 (1982).

[37] A. Karmakar and A. Ghosh, Current Applied Physics **12**, 539 (2012).

[38] D. Ray, A. Himanshu, T. Sinha, *et al.*, Indian Journal of Pure and Applied Physics **45**, 692 (2007).

[39] M. H. Harun, E. Saion, A. Kassim, M. Y. Hussain, I. S. Mustafa, and M. A. A. Omer, Malaysian Polymer Journal **3**, 24 (2008).

[40] A. Dey, S. De, A. De, and S. K. De, Nanotechnology **15**, 1277 (2004).

[41] A. K. Himanshu, R. Ray, S. El-Sayed, A. Hassen, S. K. Bandyopadhayay, and T. P. Sinha, Radiation Effects and Defects in Solids **169**, 73 (2014).

[42] S. Elliott, Advances in Physics **36**, 135 (1987).

[43] J. C. Dyre and T. B. Schrøder, Rev. Mod. Phys. **72**, 873 (2000).

[44] P. K. Karahaliou, N. Xanthopoulos, C. A. Krontiras, and S. N. Georga, Physica Scripta **86**, 065703 (2012).